THE JOURNAL OF
PHYSICAL CHEMISTRY C

Article

pubs.acs.org/JPCC

Use of the Grand Canonical Transition-Matrix Monte Carlo Method to Model Gas Adsorption in Porous Materials

Daniel W. Siderius* and Vincent K. Shen

Chemical Sciences Division, National Institute of Standards and Technology, Gaithersburg, Maryland 20899, United States

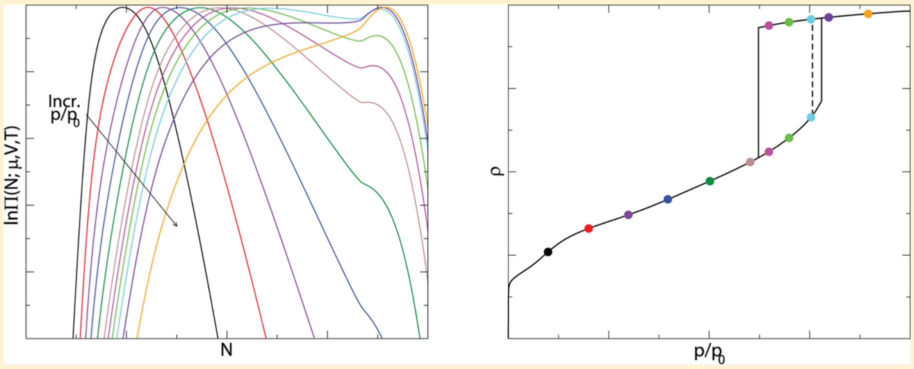

ABSTRACT: We present grand canonical transition-matrix Monte Carlo (GC-TMMC) as an efficient method for simulating gas adsorption processes, with particular emphasis on subcritical gas adsorption in which capillary phase transitions are present. As in other applications of TMMC, the goal of the simulation is to compute a particle number probability distribution (PNPD), from which thermophysical properties of the system can be computed. The key advantage of GC-TMMC is that, by appropriate use of histogram reweighting, one can generate an entire adsorption isotherm, including those with hysteresis loops, from the PNPD generated by a single GC-TMMC simulation. We discuss how to determine various thermophysical properties of an adsorptive system from the PNPD, including the identification of capillary phases and capillary phase transitions, the equilibrium phase transition, other free energies, and the heat of adsorption. To demonstrate the utility of GC-TMMC for studies of adsorption, we apply the method to various systems including cylindrical pores and a crystalline adsorbent to compute various properties and compare results to previously published data. Our results demonstrate that the GC-TMMC method efficiently yields adsorption isotherms and high-quality properties of adsorptive systems and can be straightforwardly applied to more complex fluids and adsorbent materials.

I. INTRODUCTION

As a general rule, the properties of a fluid can be altered significantly from their bulk values when confined in tight spaces, with the magnitude of such alterations dependent on the characteristics of the confining walls, specifically the affinity of the fluid to the surface.[1] Of particular scientific and technical interest is the effect of confinement on a fluid's phase behavior (or phase boundaries).[1−3] For example, fluid adsorption in porous materials, the focus of this work, serves as the basis for potential viable carbon capture technologies.[4−7] While theory and simulation have played a historically significant role in the characterization of porous materials,[1,8,9] they have more recently been identified as key tools in screening and developing potential carbon capture materials.[10−12] Thus, the advancement of carbon capture technologies and other applications of gas adsorption will depend on the availability and further development of computationally efficient and precise methods to predict the thermodynamic and dynamic properties of fluids in porous materials. At present, the two primary molecular modeling tools used in studies of adsorption are density functional theory[13] (with which we include the closely related lattice mean field theories[14−17]) and various forms of Monte Carlo (MC) molecular simulation.[18,19] These methods have proven essential to the advancement of the fundamental understanding of adsorption processes[8] by, for example, suggesting the existence of cavitation-induced capillary evaporation in ink-bottle pores prior to its observance experimentally[20] and confirming the relationship between subcritical adsorption hysteresis and fluid metastability.[21,22]

One of the main goals in the simulation of adsorption phenomena is the calculation of the adsorption isotherm, which in turn requires identifying and determining metastable and stable fluid phases. For example, in the quintessential adsorption problem at a subcritical temperature, the adsorption isotherm may include two main density branches, one that is vapor-like and the other that is liquid-like. Both branches of the isotherm will exist at some range of pressures below the bulk saturation pressure, forming a so-called hysteresis loop. Figure 1 shows an example of one such isotherm, known as a type IV isotherm,[23] in which the confined fluid exhibits two capillary

Received: January 15, 2013
Revised: February 20, 2013
Published: February 21, 2013

dx.doi.org/10.1021/jp400480q | J. Phys. Chem. C 2013, 117, 5861−5872

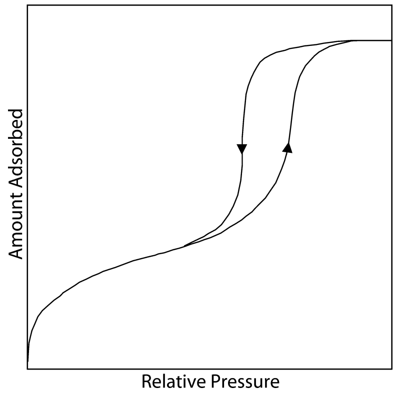

Figure 1. Type IV adsorption isotherm from the IUPAC classification scheme of 1985,[23] showing an example of adsorption/desorption hysteresis. The up and down arrows indicate the adsorbing and desorbing branches of the isotherm, respectively.

phase transitions that mark the boundaries of the hysteresis loop. While the details of the adsorptive system ultimately determine the nature of a hysteresis loop in an adsorption isotherm,[3,20−22,24,25] we may broadly attribute it to the existence of metastable states that are prolific for confined fluid systems.[21,22] Traditionally, conventional simulation methods, such as grand-canonical MC and Gibbs ensemble MC,[26−28] have been used to determine adsorption isotherms. While these methods are well suited to study thermodynamic phase equilibria, they are not as well suited to study metastable conditions, particularly near stability limits where the free energy barriers are relatively low, which are frequently encountered in the simulation of confined fluids. Other methods, such as gauge cell MC[29−31] and Wang−Landau sampling,[32−36] have emerged with some success.

Another MC technique that has proven to be efficient for and successful in the determination of phase behavior and the examination of metastable states is the transition-matrix MC (TMMC) method implemented in the grand canonical ensemble (GC-TMMC).[37−44] Some of the features of GC-TMMC that allow for accurate examination of metastable states are (1) its goal of calculating the particle number probability distribution (PNPD) instead of direct calculation of ensemble averages and (2) a biasing scheme that encourages the simulation to sample all states (stable, metastable, and unstable) equally, i.e., via a flat histogram of visited states. Most important, however, is that one can exploit histogram reweighting of the PNPD at one thermodynamic state point to generate that of another state point, without running an additional simulation. Via the newly generated PNPD, one can generate any of the ensemble averages and thermophysical properties that were obtained from the original PNPD. Thus, a single GC-TMMC simulation can produce an entire adsorption isotherm while also identifying the conditions of phase coexistence, limits of stability, and various other properties of interest, at a particular temperature. We note that GC-TMMC has been applied to adsorptive systems,[45−48] but it has not been used to identify metastable stables nor has it been used to construct isotherms with hysteresis. Here we introduce the use of GC-TMMC and the analysis of its simulation output as a method for studying adsorption and aim to promote it as a complement to existing molecular modeling techniques.

This paper is organized as follows. In section II, we present the essential details of the GC-TMMC method. Section III discusses our methodology for generating a number of adsorption-related thermophysical properties from a single PNPD obtained via GC-TMMC simulation. In section IV, we describe the model adsorption systems that were simulated for the present work. We present examples of TMMC-generated adsorption isotherms and various other properties in section V, which also includes some comparisons to simulation and experimental results in the extant literature. The paper is concluded in section VI with a summary of our application of GC-TMMC to adsorption problems and a discussion of its key benefits.

II. GRAND CANONICAL TRANSITION-MATRIX MONTE CARLO METHOD

We begin by presenting some important details of the GC-TMMC simulation algorithm that we aim to introduce for application in simulation of adsorption hysteresis. TMMC traces back to a method originally introduced by Fitzgerald et al.,[37,38] though we use a modified form of TMMC pioneered by Errington and co-workers; for a full discussion of the method, consult refs 39−44. The main difference between the two variants of TMMC is Errington's incorporation of a biasing function (see below) that improves sampling of unlikely configurations.

The main objective of a GC-TMMC simulation is to calculate the particle number probability distribution, $\Pi(N; \mu, V, T)$, which is the probability of observing N particles (or atoms or molecules depending on the simulated species) in an ensemble of volume V at fixed temperature T and chemical potential μ. The set of configurations with their number of particles equal to N is said to comprise a macrostate within the ensemble, and the macrostate probability or PNPD in the GC ensemble is given by

$$\Pi(N; \mu, V, T) = \frac{\exp(\beta\mu N)Q(N, V, T)}{\Xi(\mu, V, T)} \tag{1}$$

$Q(N, V, T)$ and $\Xi(\mu, V, T)$ are the canonical and grand canonical partition functions, respectively, $\beta = 1/k_BT$ (in which k_B is Boltzmann's constant[49]), and all other terms are as previously defined. In a conventional grand canonical Monte Carlo (GCMC) simulation, this distribution can be determined by constructing a histogram. In contrast, TMMC utilizes statistics regarding attempted transitions to determine $\Pi(N; \mu, V, T)$. This is done by accumulating information within a collection matrix $\mathbf{C}$ according to

$$\begin{aligned} C(N_o \to N_n) &= C(N_o \to N_n) + p_{acc}(o \to n) \\ C(N_o \to N_o) &= C(N_o \to N_o) + 1 - p_{acc}(o \to n) \end{aligned} \tag{2}$$

where the labels o and n identify the old and new configurations for the attempted transition and p_{acc} is the acceptance probability for the attempted transition. The collection matrix $\mathbf{C}$ is updated (see eq 2) after each MC trial move, regardless of whether the move is actually accepted. In GC-TMMC, one usually restricts the simulation to three types of single-molecule trial moves: translations, insertions, and deletions. Thus, the $\mathbf{C}$ matrix is triply banded, i.e., the only possible transitions are $N \to N + \delta$, where $\delta = -1, 0$, or $+1$. The acceptance probability of a trial move may be written as[50,51]

$$p_{acc}(o \to n) = \min\left[1, \frac{\alpha(n \to o)\pi_n}{\alpha(o \to n)\pi_o}\right] \tag{3}$$

where $\alpha(\mathrm{o} \rightarrow \mathrm{n})$ is the probability of generating configuration n from configuration o and π_{o} is the probability of configuration o. We have written the term p_{acc} in eq 3 as generically as possible so that it can accommodate any type of Monte Carlo move consistent with the chosen ensemble constraints.

From the collection matrix, one may then compute the probability transition matrix, **P**, according to

$$P(N \rightarrow N + \delta) = \frac{C(N \rightarrow N + \delta)}{\sum_{j=-1}^{+1} C(N \rightarrow N + j)} \tag{4}$$

Finally, since **P** is triply banded, one can invoke detailed balance to yield a relationship between Π and **P**:

$$\begin{aligned} &\ln \Pi(N + 1; \mu, V, T) \\ &= \ln \Pi(N; \mu, V, T) + \ln\left[\frac{P(N \rightarrow N + 1)}{P(N + 1 \rightarrow N)}\right] \end{aligned} \tag{5}$$

Equation 5 provides a unique solution for Π, which is obtained by fixing Π to an arbitrary value at some $N_{\min}$ and then sequentially calculating $\Pi(N_{\min} + 1; \mu, V, T)$, $\Pi(N_{\min} + 2; \mu, V, T)$, etc. The PNPD can then be normalized, if desired. Finally, the bounds of N, $N_{\min}$, and $N_{\max}$ are selected so that the simulation samples the desired part of the macrostate domain. For reasons that we will discuss later, it is valuable to select $N_{\min} = 0$. $N_{\max}$ should be selected to ensure that $\Pi(N; \mu, V, T)$ has a low probability tail at $N_{\max}$.[40]

For GC-TMMC to satisfactorily compute Π, it must sample all relevant N-macrostates so that sufficient statistics for **C** are collected. In a normal GCMC simulation, the system tends to sample only values of N near a local maximum of the PNPD for the imposed (μ, V, T). To encourage the sampling of a broader range of N values, Errington proposed that a biasing function, $\eta(N)$, be incorporated into the TMMC algorithm to encourage uniform sampling of all macrostates.[39] In this scheme, MC trial moves are accepted according to

$$p_{\mathrm{bias}}(\mathrm{o} \rightarrow \mathrm{n}) = \min\left[1, \frac{\exp[\eta(N_{\mathrm{n}})]}{\exp[\eta(N_{\mathrm{o}})]} \frac{\alpha(\mathrm{n} \rightarrow \mathrm{o})\pi_{\mathrm{n}}}{\alpha(\mathrm{o} \rightarrow \mathrm{n})\pi_{\mathrm{o}}}\right] \tag{6}$$

It is important to note that, while eq 6 controls the actual transitions between trial configurations in the GC-TMMC simulation, the **C** matrix is still updated using the unbiased acceptance probability given in eq 3. In common with most multicanonical sampling schemes where uniform sampling is desired, the biasing function should be given by[52]

$$\eta(N) = -\ln \Pi(N; \mu, V, T) \tag{7}$$

Since the PNPD is not (usually) known *a priori*, a GC-TMMC simulation is initialized with a uniform $\eta(N)$ and begins sampling according to the uniform bias (i.e., normal GCMC). Periodically throughout the simulation, the transition statistics collected in **C** are used to compute an estimate of $\Pi(N; \mu, V, T)$ and, thereby, a new $\eta(N)$. The simulation then continues according to the new bias, which encourages more frequent sampling and collection of statistics for lower probability states. This process is repeated over the course of the simulation, with each successive recalculation of the PNPD yielding a better biasing function, which encourages sampling with greater uniformity in the next simulation segment. Thus, the biasing function self-corrects itself over the course of the simulation until the estimate of $\Pi(N; \mu, V, T)$ converges and uniform sampling is effectively achieved. We note that the goal of achieving uniform sampling is the common feature of the flat-histogram family of MC methods and that other flat-histogram sampling methods can also be used to determine the PNPD. Regardless of the method, only one simulation is required to generate an entire adsorption isotherm.

III. CALCULATION OF THERMOPHYSICAL PROPERTIES FROM $\Pi(N; \mu, V, T)$

In the following sections, we discuss a methodology for processing results from a single GC-TMMC simulation to yield a number of adsorption-related thermophysical properties. The beginning point for this process is identification of confined phases from the PNPD, after which calculation of other properties is fairly straightforward. To aid our discussion, we will present example PNPDs that were obtained via GC-TMMC but in a qualitative context only. The source of the PNPDs will be described later. An example PNPD, plotted as $\ln \Pi$ versus N is shown in Figure 2a. For various reasons and in common with most uses of TMMC, we find it useful to store and operate on $\ln \Pi$ rather than Π itself.

A. Identification of Capillary Phases and Histogram Reweighting. The beginning point for assembling an adsorption isotherm using a PNPD is to identify which phase or phases exist for a particular (μ, V, T) state point and then assign macrostates to the respective phase(s). As in other

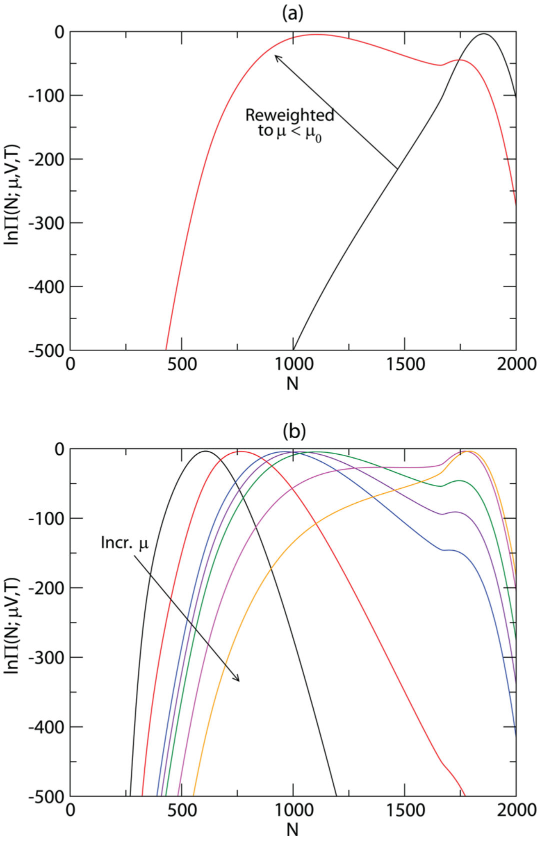

Figure 2. (a) Particle number probability distributions for the Ar–MWCNT system with radius 3.935 nm and length 2.043 nm at T = 87.3 K. The black line corresponds to p/p_0 = 12.67, and the red line corresponds to p/p_0 = 0.700. (b) Particle number probability distributions for the same system for μ corresponding to p/p_0 = 0.20, 0.40, 0.60, 0.65, 0.70, 0.80, and 0.90. The arrow indicates the direction of increasing μ or, equivalently, pressure.

applications of GC-TMMC involving multiphase systems, each local maximum in Π (or $\ln \Pi$) identifies a stable phase, to which some or all of the sampled macrostates belong.[39−41] For the trivial case in which there is a single maximum, the state point contains a single phase and all macrostates belong to that phase, such as the case shown by the black line in Figure 2a. If two local maxima exist, as shown by the red line in Figure 2a, then the local minimum between the maxima is selected as the point that divides the distribution into two phases; i.e., states with N below the local minimum belong to the low density phase and vice versa for the high density phase.[40] Designating one of the phases as α, the density of that phase can be calculated by

$$\langle \rho_\alpha \rangle = \frac{1}{V} \frac{\sum_{N\in\alpha} N\Pi(N; \mu, V, T)}{\sum_{N\in\alpha} \Pi(N; \mu, V, T)} \tag{8}$$

where the sums are over the macrostates that belong to phase α and V is the relevant volume. For the present discussion and for simplicity, we chose V to be the total volume of the confining pore. This methodology can easily be extended to systems with more than two phases, where the division between phases always occurs at a local minimum in Π.

As mentioned earlier, one of the major strengths of GC-TMMC is that the PNPD computed at one μ value can, by use of histogram reweighting, yield thermodynamic information for other μ values; additional simulations are not necessary. By recognizing that $Q(N, V, T)$ is not dependent on μ, eq 1 can be manipulated to yield

$$\begin{aligned} &\ln \Pi(N; \mu, V, T) \\ &\quad = \ln \Pi(N; \mu_0, V, T) + \beta N(\mu - \mu_0) + C \end{aligned} \tag{9}$$

where C is a normalization constant independent of N. Equation 9 is, then, a prescription for reweighting a PNPD at μ_0 to some other μ, with no need for additional simulation effort. As an example, Figure 2a also contains $\ln \Pi$ (shown in red) that has been obtained by reweighting the source PNPD (black) to a lower μ. At this new state point, $\ln \Pi$ exhibits two local maxima corresponding to the vapor and liquid capillary phases, with the division between phases falling at the local minimum between the two maxima. Figure 2b displays several PNPDs obtained by reweighting the source PNPD to various values of μ, compactly showing the system's progression from a single vapor-like phase to two coexisting phases and finally a single liquid-like phase. Repeated reweighting of the PNPD allows one to compute an entire adsorption isotherm from the PNPD from a single GC-TMMC simulation. In addition, the ability to reweight Π makes the selection of μ largely immaterial, provided that the simulation samples the macrostates corresponding to relevant vapor and liquid densities and that Π has low probability tails at its lower and upper bounds.

B. Capillary Phase Transitions. In the previous section, we associated individual capillary phases with local maxima in Π and selected the local minimum between two local maxima as the dividing point between those two phases. While this division of the PNPD into two (or more) phases is intuitive and appealing for its simplicity, it is also well-founded in thermodynamics and thermodynamic stability analysis. To begin, we must recall that the two-phase region of a subcritical adsorption isotherm (the hysteresis loop) is bounded by capillary phase transitions at two different pressures. Capillary evaporation is at the low-pressure bound of the two-phase region and capillary condensation is at the high-pressure bound. For the infinite-length pores we examine in this work, both capillary phase transitions occur at thermodynamic limits of stability (spinodal points).[53] (For finite-length pores that directly contact a gas-phase reservoir, the evaporation transition occurs at the equilibrium phase transition.[3,21,22,53])

From a kinetic point of view, a limit of stability is identified by the vanishing of the free energy barrier between two phases. For a system at fixed (μ, V, T), the free energy of a particular N macrostate, $W(N; \mu, V, T)$, may be related to the PNPD via[41]

$$W(N; \mu, V, T) = -kT \ln \Pi(N; \mu, V, T) \tag{10}$$

For the two-phase systems of interest, W as computed from eq 10 will have two local minima separated by a local maximum. The lower free energy minimum is the stable equilibrium state, and the higher minimum is the metastable state. Correspondingly, the free energy barrier between the metastable and stable states is[41]

$$\begin{aligned} \Delta W(\mu, V, T) &= W(N_b; \mu, V, T) \\ &\quad - W(N_{ms}; \mu, V, T) \end{aligned} \tag{11}$$

$$= -kT \ln \frac{\Pi(N_b; \mu, V, T)}{\Pi(N_{ms}; \mu, V, T)} \tag{12}$$

where N_b and N_{ms} are the particle number macrostates corresponding to the local maximum in W and the metastable state, respectively. Hence, a limit of stability or $\Delta W \rightarrow 0$ appears when the local maximum at N_b merges with the local minimum at N_{ms}. Additionally, this kinetic definition implies that a limit of stability occurs at a μ_{spin} for which $\ln \Pi(N; \mu_{spin}, V, T)$ contains a saddle point, e.g., where a local maximum has disappeared. Thus, use of the simple criteria selected in section IIIA to identify multiple phases in Π yields boundaries of the two-phase region that are consistent with the kinetic definition of spinodal points corresponding to the capillary phase transitions. Figure 3 plots $\ln \Pi$ characteristic of two capillary phase transitions for a confined fluid system, one corresponding to a capillary condensation event and the other to capillary evaporation. The plot is a clear illustration of the coincidence of a limit of stability with a μ state point whose PNPD contains a saddle point.

C. Equilibrium Phase Transition (Phase Coexistence). An additional adsorption property that is straightforwardly obtained from the PNPD is the location of the equilibrium phase transition, defined by equality of the grand free energy of the two capillary phases[3,22,53] at a given temperature. This is equivalent to the conditions of phase coexistence or a binodal point. If, for example, one traced through the state points in the adsorption isotherm shown in Figure 4 and jumped from the vapor branch of the isotherm to the liquid branch at the p/p_0 corresponding to the equilibrium phase transition, the trace would pass through the stable equilibrium states exclusively.

The grand free energy for phase α, Ω_α, may be computed via[28,40−43,54,55]

$$\beta\Omega_\alpha = \ln \Pi(0; \mu, V, T) - \ln\Big[\sum_{N\in\alpha} \Pi(N; \mu, V, T)\Big] \tag{13}$$

The summation on the right side of eq 13 is identical to the denominator of eq 8 which allows the grand free energy to be easily computed in tandem with the adsorption isotherm, provided that the $N = 0$ state has been adequately sampled. The

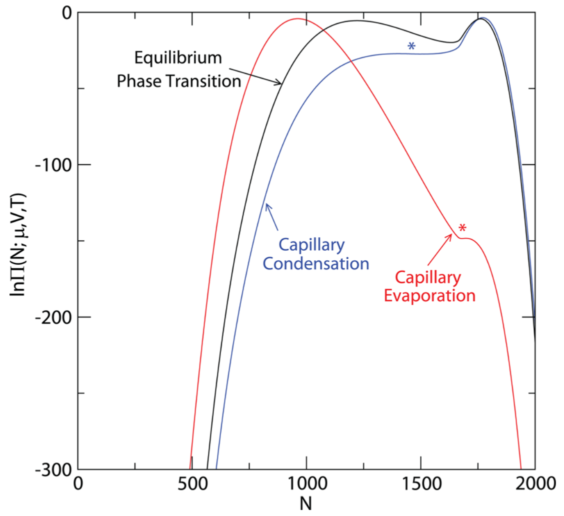

Figure 3. Particle number probability distributions for the Ar−MWCNT system with radius 3.935 nm and length 2.043 nm at 87.3 K reweighted to state points at the limits of stability and the equilibrium phase transition. The blue line identifies ln Π at the capillary condensation transition (vapor spinodal at $z\sigma_{\text{Ar}}^3 = 0.01571$ or $p/p_0 = 0.7988$), the red line identifies the capillary evaporation transition (liquid spinodal at $z\sigma_{\text{Ar}}^3 = 0.01204$ or $p/p_0 = 0.5939$), and the black line identifies the equilibrium phase transition ($z\sigma_{\text{Ar}}^3 = 0.01498$ or $p/p_0 = 0.7569$). The saddle points in ln Π at the spinodal conditions are marked with an asterisk.

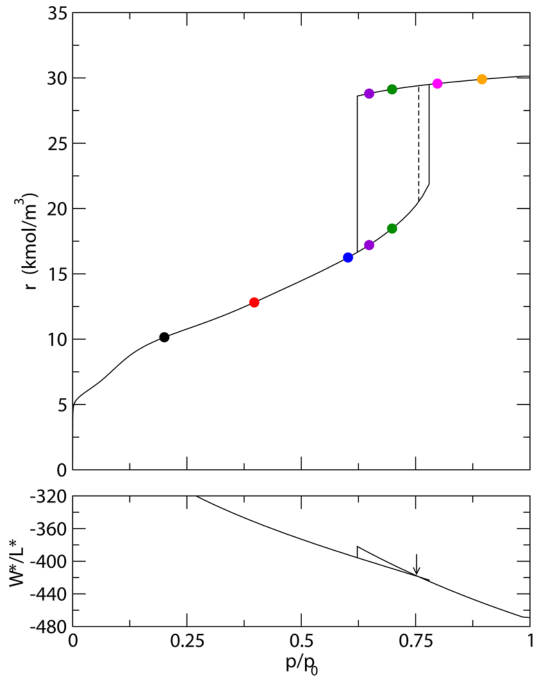

Figure 4. (top) Adsorption isotherm for the Ar−MWCNT system with radius 3.935 nm and length 2.043 nm at $T = 87.3$ K. Solid circles indicate the state points at $p/p_0 = 0.20$, 0.40, 0.60, 0.65, 0.70, 0.80, and 0.90, and the color codes match those in Figure 2b. p_0 is the bulk saturation pressure. The solid black line is the locus of adsorbed densities computed by histogram reweighting of ln Π at 1000 μ points. The dashed black line identifies the equilibrium phase transition. (bottom) Grand free energy per unit length for the same Ar−MWCNT system, in reduced units. The small arrow indicates the equilibrium phase transition, where the grand free energies of the vapor and liquid phases are equal, in this case $p/p_0 = 0.7568$.

dependence of Ω on $\Pi(0;\mu,V,T)$ is the reason that we select $N_{\min} = 0$ when setting the macrostate bounds for the simulation.

One could graphically inspect a plot of Ω to find the pressure or chemical potential at which the grand free energy of the vapor and liquid phases is equal, e.g., $\Omega_{\text{vap}} = \Omega_{\text{liq}}$. For a more precise calculation, one can apply this equality criteria to eq 13 to yield the following condition on Π at the equilibrium phase transition:

$$\sum_{N\in\text{vapor}} \Pi(N;\mu_{\text{bin}},V,T) = \sum_{N\in\text{liquid}} \Pi(N;\mu_{\text{bin}},V,T) \tag{14}$$

μ_{bin} is the chemical potential that corresponds to the equilibrium phase transition or binodal. Hence, the equilibrium phase transition may be located by searching for a μ that yields a reweighted Π that satisfies eq 14. One could use an advanced numerical search technique to do so, but we find that it is quite satisfactory to solve for μ_{bin} for a single component system using the conventional bisection method with the two limits of stability as initial guesses for the lower and upper search bounds. Figure 3 contains an example plot of the PNPD that was reweighted such that eq 14 is satisfied. Additionally, we note that the condition in eq 14 applies to the sum of Π over all macrostates in each phase and does not generally imply that the values of the PNPD at the two local maxima are equal.

D. Other Ensemble Properties: Isosteric Heat of Adsorption. Beyond its application for computing isotherms and identifying phase transitions, GC-TMMC can also compute ensemble averages of other properties that may be of interest. We first note that ensemble averages of a generic quantity, A, in the GC ensemble may be computed for phase α by

$$\langle A_\alpha\rangle = \frac{\sum_{N\in\alpha} A(N,V,T)\Pi(N;\mu,V,T)}{\sum_{N\in\alpha}\Pi(N;\mu,V,T)} \tag{15}$$

Beyond the results provided by the core GC-TMMC algorithm, eq 15 only requires that the GC-TMMC simulation accumulate an average of $A(N,V,T)$ for each N macrostate visited by the simulation.

To illustrate the use of eq 15, here we consider the isosteric enthalpy of adsorption (e.g., a so-called "heat of adsorption"), which is the enthalpy change associated with the transferal of a molecule from the bulk reservoir to an adsorbed phase. Many different definitions are available,[56−58] but we chose that obtained by Do et al.[57,58]

$$Q_{\text{st}} = \frac{\langle N_{\text{g}}\rangle kT}{f(N_{\text{g}},N_{\text{g}})} - \frac{f(U,N)}{f(N,N)-f(N_{\text{g}},N_{\text{g}})} \tag{16}$$

in which Q_{st} is the isosteric enthalpy of adsorption, U is the internal energy, N is the number of molecules in the system, and N_{g} is the number of molecules in a bulk system at the same pressure (chemical potential) and the same accessible volume as the confined system. In eq 16, f represents a fluctuation quantity defined by

$$f(A,B) = \langle AB\rangle - \langle A\rangle\langle B\rangle \tag{17}$$

in which A and B are generic observables in the simulation. The average quantities in eq 17 can be computed using eq 15 provided that canonical averages of A, B, and AB are computed for each N. Computation of Q_{st} is then extraordinarily simple in GC-TMMC, as the only necessary addition to the simulation is the accumulation of $U(N, V, T)$ that can be averaged at simulation end; all other terms in eq 16 are available directly from the PNPD of either the adsorptive system or the bulk fluid that is used to compute the chemical potential-pressure relationship.

IV. COMPUTATIONAL DETAILS

In the next section, we will present results from GC-TMMC simulations of gas sorption in four adsorptive systems: argon (Ar) in two types of multiwall carbon nanotube (MWCNT) adsorbents, Ar in a cylindrical-shaped pore bored through solid CO_2, and CO_2 in a metal organic framework known as ZIF-8 (described below). Due to the difference in complexity of the adsorbates, the MC strategies for the various adsorbents differed.

In our simulations of Ar in the noted porous adsorbents, the Ar–Ar interaction was modeled by the Lennard-Jones (LJ) potential truncated by a linear-force shift at a specified cutoff radius, r_{cut}.[18] The first MWCNT adsorbent we examined was modeled by the Cylindrical Steele 10-4-3 (CS 10-4-3) potential,[59] which represents a MWCNT composed of many CNT layers. The second MWCNT adsorbent we examined was one composed of three concentric CNT layers[60,61] separated by an interlayer distance Δ (see Table 1). Each CNT layer was individually modeled by the Cylindrical LJ 10-4 (CLJ 10-4) potential[62] and summed to obtain the net adsorbate–adsorbent interaction. In our third model system, the interaction between Ar and solid CO_2 was modeled by the Cylindrical LJ 9-3 (CLJ 9-3) potential.[63,64] (The second and third fluid–sorbent systems were chosen to facilitate comparison of our results with those in refs 60 and 65.) LJ interaction parameters for the Ar–Ar interaction and Ar–sorbent cross-interaction are given in Table 1. Simulations were performed for various radii of cylindrical pores with axial lengths equal to at least $2r_{\text{cut}}$ (usually larger). Periodic boundary conditions were applied in the axial direction. To increase the efficiency of GC-TMMC, we implemented the algorithm using a "divide and conquer" strategy, where the N domain is divided into some number of overlapping subdomains and each subdomain is investigated by an independent simulation.[45] Simulation of the LJ-type fluid were run for 3×10^{10} trial moves, with 40% of the moves being displacements and the remainder split evenly between insertions and deletions and the biasing function was updated after every 10^6 trial moves. [We note that this simulation run-time is much longer than a normal GCMC simulation (about 1×10^7 trial moves per state point). This was done to obtain low-uncertainty results that will be used as reference data in the future.] The PNPDs for the overlapping subdomains were combined following completion of the entire group of simulations to yield a single PNPD for the entire N domain. Since it can be difficult to insert particles at high density, we adopted the method of expanded ensembles[66,67] for the GC particle insertion/deletion moves. In our simulation, insertions (deletions) are done by growing (shrinking) the LJ σ stepwise through a sequence of stages,[68−70] each of which has a reasonable energy cost compared to inserting (deleting) the full-size LJ particle.

Table 1. Lennard-Jones Parameters and Relevant Physical Properties for the Ar–Ar Fluid Interaction, Ar–Carbon Solid–Fluid Interaction, and Ar–CO_2 Solid–Fluid Interaction[a]

interaction	σ (nm)	ϵ/k_B (K)	ρ_S (nm^{-3})	Δ (nm)	refs
Ar–Ar	0.3405	119.8			79, 80
Ar–C	0.3403	57.92	114.0	0.3350	81
Ar–CO_2	0.3725	153.0	20.94		65, 82

[a] σ is the LJ diameter, ϵ is the LJ energy scale, and k_B is Boltzmann's constant.[49] The cross interaction parameters were derived via Lorentz–Berthelot mixing rules. In the CS 10-4-3 and CLJ 9-3 potentials, ρ_S is the density of the solid adsorbent. ρ_S for CO_2 is increased approximately 10% above its literature value, as in ref 65. Δ is the spacing between graphite basal layers used in the CS 10-4-3 potential. For the CLJ 10-4 potential, the areal (surface) density ρ_A is equal to $\rho_S \cdot \Delta$.

The fourth system chosen was the adsorption of CO_2 in the zeolitic imidazolate framework (ZIF) bis(2-methylimidazolyl)-zinc ($C_8H_{10}N_4Zn$), typically denoted ZIF-8. The ZIF-8 structure was reconstructed from X-ray powder diffraction measurements[71] and was represented in our simulation as a supercell of eight crystal unit cells (a cube with side length 3.4023 nm) with periodic boundary conditions applied in all directions. We modeled CO_2 using the TraPPE forcefield[72] (three LJ sites and three point charges, rigid atomic bonds) and modeled the interaction between CO_2 and the atomic members of ZIF-8 using the force field given by Perez-Pellitero et al.,[73] which was tuned for simulation of gas sorption in ZIF materials. The LJ potentials were truncated at 1.5 nm with a linear-force shift. Electrostatic interactions were evaluated by the standard Ewald summation method with tinfoil boundary conditions and truncation of the real-space term at 1.5 nm. The damping parameter used was $\alpha \times L = 5.6$, where L is the smallest periodic dimension of the simulation cell, and the maximum number of Fourier-space vectors was set by $k_{\max} = 5$. The simulation was run for 1×10^9 trial moves, with 30% of moves being displacements, 20% being rotations about the CO_2 center of mass, and the remainder split between insertions and deletions. All MC moves for the TraPPE CO_2 simulation were done using an orientation-bias scheme, essentially identical to configurational-bias MC (CBMC),[74−78] where several orientations of CO_2 were proposed for each trial move and CBMC sampling was used to select one of the proposed orientations. The CBMC-related steps in our MC software were parallelized using OpenMP to expedite simulation.

Lastly, GC-TMMC simulations of the unconfined adsorbate fluids were performed to determine equations of state relating the imposed chemical potential to an equivalent pressure and bulk gas density. The bulk simulations were done in cubic boxes of volume $V = 512\sigma_{\text{Ar}}^3$ and $V = 27$ nm^3 for LJ Ar and TraPPE CO_2, respectively, with other parameters identical to those of the confined fluid simulations, unless otherwise specified.

V. EXAMPLE APPLICATIONS

Having established a methodology for using GC-TMMC to obtain adsorption isotherms, we can now turn to some example applications to demonstrate and validate its use. The following examples apply the GC-TMMC method discussed in section II to the three adsorptive systems described above.

A. Ar–MWCNT (1). To begin, we present a series of results for Ar–MWCNT systems to demonstrate how to generate an adsorption isotherm using GC-TMMC. Figure 2a contains the PNPD generated by GC-TMMC simulation of Ar in a MWCNT of inner radius 3.935 nm with axial length $6\sigma_{\text{Ar}}$ at $T = 87.3$ K. The radius corresponds to that of a (58,58) carbon nanotube,[83] and the temperature is the normal boiling temperature of Ar, which is also the standard temperature for use of Ar in porous materials characterization.[3] For this demonstration of GC-TMMC, we truncated and linear-force-shifted the fluid–fluid potential at $r_{\mathrm{cut}} = 2.5\sigma_{\mathrm{Ar}}$[18] and ran the base simulation at the reduced activity $z\sigma_{\mathrm{Ar}}^3 = \exp(\beta\mu)/(\Lambda/\sigma_{\mathrm{Ar}})^3 = 0.02705$ (Λ is the thermal de Broglie wavelength), corresponding to the reduced pressure $p/p_0 = 12.67$ (far into the liquid state of the bulk fluid at this temperature). The high activity aided sampling of high-N macrostates in the TMMC simulation. Macrostate bounds for the simulation were set to $N_{\min} = 0$ and $N_{\max} = 2080$, and a short test simulation confirmed that this $N_{\max}$ was sufficiently large to yield a low probability tail in Π. Figure 2b contains PNPDs for the same system at various reduced pressures below the bulk saturation pressure, p_0, and Figure 3 contains the PNPDs corresponding to the capillary and equilibrium phase transitions. From these PNPDs and using the phase identification procedure described above, we computed the isotherm shown in Figure 4, where the symbols were obtained from the PNPDs in Figure 2b. The remainder of the isotherm, shown by a black line, is the locus of densities generated by reweighting Π to 1000 different μ state points. For this case, we have plotted the average pore density based on the total volume definition of ρ. The bottom panel of Figure 3 displays the grand free energy of the system, and the equilibrium phase transition is identified by a small arrow. For this particular system, the equilibrium phase transition occurs at $p/p_0 = 0.7568$.

In addition to the 3.935 nm MWCNT system, we performed GC-TMMC simulations for Ar–MWCNT systems for four additional inner radii: 1.357, 2.036, 2.646, and 3.053 nm. [These radii correspond to (20,20), (30,30), (39,39), and (45,45) carbon nanotubes,[83] respectively.] The axial length was $12\sigma_{\mathrm{Ar}}$ for the two smallest radii and $6\sigma_{\mathrm{Ar}}$ for the other radii. All simulations were run at $z\sigma_{\mathrm{Ar}}^3 = 0.02705$ (as before) and sampled from $N_{\min} = 0$ to an $N_{\max}$ value that yielded a maximum reduced density of about 0.90. The resultant isotherms, along with that from the 3.935 nm radius system, are shown in Figure 5. Similar to the isotherm for 3.935 nm, the isotherms for 2.646 and 3.053 nm are the standard type IV isotherms expected for subcritical adsorption in mesopores with relatively strong fluid–solid interactions. The two smallest radii, however, do not exhibit hysteresis, from which we can conclude that the critical diameter for this system at 87.3 K is between 2.036 and 2.646 nm. (Alternatively, the critical hysteresis temperature is below 87.3 K for the smallest radii.) In all five cases shown, a complete monolayer forms at low pressure (approximately $p/p_0 = 0.001$, as determined from a log-scale plot). For the smallest radii, a succession of additional layers forms as pressure increases, until the pore is virtually filled at $p/p_0 = 0.3$. For the remaining sizes, the pores infill slowly until a liquid-like density is reached via a continuous transition (for the 2.036 nm pore) or capillary condensation. In this particular model, the isotherms do not exhibit "steps" that are indicative of the formation of successive monolayers on a smooth, homogeneous surface. This is a consequence of our choice of r_{cut}. Use of a longer cutoff radius such as $4\sigma_{\mathrm{Ar}}$ restored the formation of distinct monolayers. Lastly, the equilibrium phase transitions for the three largest radii appear very close to the capillary condensation step. This too was a consequence of the small cutoff radius. We note that these results (along with those in Figures 7 and 8) demonstrate the value of using rigorous calculations to locate the equilibrium phase transition. One may be tempted to estimate its position at the midpoint between the two limits of stability, but our results indicate that such an expectation may prove incorrect.

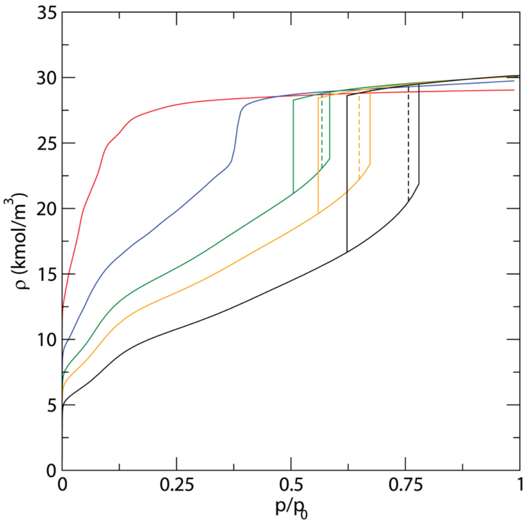

Figure 5. Adsorption isotherms for Ar–MWCNT systems with radius 1.357 nm (red), 2.036 nm (blue), 2.646 nm (green), 3.053 nm (orange), and 3.935 nm (black), computed at 87.3 K using the GC-TMMC method described in the text. ρ is the average volume of Ar in the pore, based on the total volume definition, and p is the gas pressure. p_0 is the bulk saturation pressure for the specified temperature. The equilibrium phase transition for systems exhibiting hysteresis is shown by a dashed line of the same color as the isotherm.

To further illustrate the utility of GC-TMMC for computing adsorption quantities (or properties) for systems with hysteresis, we now examine the isosteric heat of adsorption for the MWCNT pores discussed above. Historically, the quality of computational calculations of Q_{st} has been much poorer than that of an isotherm, most likely due to greater challenge of computing fluctuation quantities. GC-TMMC, on the other hand, may provide higher quality calculations of fluctuation quantities, since the necessary ensemble averages are computed indirectly via the PNPD. Figure 6 contains Q_{st} calculations for the Ar–MWCNT systems whose isotherms are displayed in Figure 5. In this figure, we have only shown Q_{st} for stable states; i.e., for the three systems that exhibit hysteresis, the plot jumps from the vapor to liquid branches at the binodal. The resultant plots of Q_{st} are extraordinarily smooth compared to similar plots generated by conventional GCMC, particularly in the middle-density pore-filling region and on the liquid branches (e.g., see Figure 11 of ref 60). This is likely due to GC-TMMC's use of the actual PNPD to compute the $f(U, N)$ and other fluctuation quantities, which must be computed using a well-tuned block averaging scheme in a conventional MC simulation. While these smoother Q_{st} results are unlikely to lead to qualitatively different conclusions than those from a conventional MC simulation, the removal of a significant amount of noise from Q_{st} calculations may make fine details more visible. For the case in Figure 6, the general shape of the Q_{st} curves is as expected, with a prominent peak at low density (corresponding to complete formation of the first adsorbed monolayer), largely unchanging Q_{st} as the pores infill, and a sharp rise when pore filling is complete. For the two smallest radii (those without hysteresis), Q_{st} contains a second high energy peak, which indicates that a second distinct monolayer has formed. (A second peak is present for the other radii but at

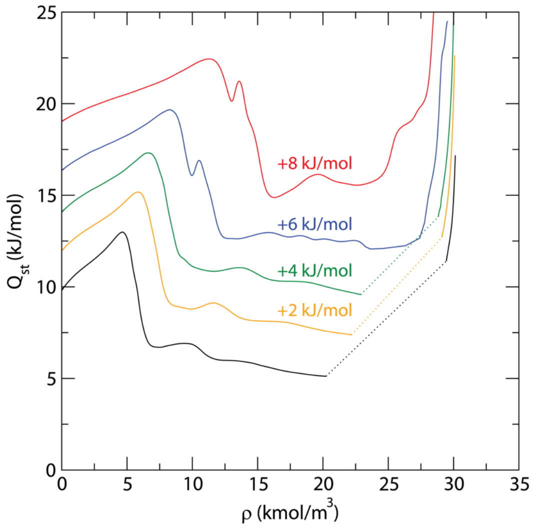

Figure 6. Isosteric heat of adsorption (Q_{st}) for Ar−MWCNT systems computed at 87.3 K using GC-TMMC and eq 16 plotted versus the average Ar density in the pore. Line colors correspond to radii as in Figure 5. All lines save that for R = 3.935 nm have been vertically shifted by the amount noted in the figure. The dotted lines are an aid to the eye that connect the stable vapor and stable liquid branches of Q_{st} for the three systems that exhibit hysteresis.

lower energy, indicating that the monolayer is more diffuse than the layer closest to the MWCNT surface.) This feature is not obvious in the isotherms for those radii and is a simple illustration of the extra insight obtained by calculation of Q_{st} in tandem with an adsorption isotherm.

We examined the statistical variation of adsorption properties of these Ar−MWCNT systems by analyzing the results of four repeat GC-TMMC simulations of the R = 2.646 nm system using appropriate statistical tests. Each independent batch of simulations (e.g., the set of simulations for the "divide and conquer" strategy) was initialized from a different configuration with a different seed integer for the random number generator and run as described above. Then, the adsorption analysis described in section III was applied to the four PNPDs to yield the various adsorption properties described in the present text, after which we computed the 95% confidence intervals for those properties to be used as estimates of the statistical uncertainty. Overall, the adsorption isotherms generated by GC-TMMC have very low uncertainties. We observe the largest relative uncertainties, up to 4.27%, at very low p/p_0. For nominal pressures ($p/p_0 > 0.0005$), the relative uncertainty is of the order 0.1% or smaller. Relative uncertainties for the p/p_0 locations of the equilibrium phase transition, vapor stability limit (capillary evaporation), and the liquid stability limit (capillary condensation) are 2.881×10^{-4}, 3.380×10^{-4}, and 1.084×10^{-3}, respectively. In all cases, the uncertainty in the location of these phase properties is low in both real and relative terms, as the relative uncertainties are less than 0.1% at the equilibrium phase transition and condensation spinodal and still only 0.22% at the evaporation spinodal. Lastly, we find that the relative uncertainty in the isosteric heat is somewhat larger than that in the properties already mentioned. The maximum uncertainty in Q_{st} was 1.300 kJ/mol at ρ = 30.09 kmol/m_3 (p/p_0 = 0.9961), corresponding to a relative error of 5.38%; this is also the largest relative uncertainty observed in Q_{st}. For vapor densities, however, the maximum uncertainty was only 0.2684 kJ/mol and the maximum relative uncertainty (at a different p/p_0) was 3.58%. An examination of the simulation data showed that the larger errors in Q_{st} followed from larger variation in $U(N, V, T)$ at the highest density macrostates. Overall, the GC-TMMC method yields very consistent results across multiple simulations, leading to acceptable uncertainties in the adsorption properties computed from the PNPD and other ensemble averages.

B. Ar−MWCNT (2). To demonstrate the consistency of GC-TMMC with conventional GCMC, we performed simulations of an Ar−MWCNT adsorptive system that was recently investigated by Wang et al.[60] As mentioned previously, the MWCNT adsorbent was composed of three concentric CNT layers with interlayer spacing Δ = 0.3354 nm,[61] and the LJ and CLJ 10-4 potentials were used with the parameters in Table 1. The cylindrical radius was set to 2.20 nm and the axial length to 4.4 nm, and the Ar−Ar interactions were cut and shifted at 2.20 nm, as in ref 60. GC-TMMC simulations were performed at T = 87.3 K with $N_{\min}$ = 0 and $N_{\max}$ = 1350 at $z\sigma_{Ar}^3$ = 0.001708 (p = 53.38 kPa, p/p_0 = 0.5594) to obtain $\Pi(N; \mu, V, T)$. The adsorption isotherm generated from the GC-TMMC PNPD is shown in Figure 7 along with the isotherm generated by conventional GCMC presented in Figure 12 of ref 60. For both isotherms, the average density is based on the accessible volume definition of ρ using R = 1.90 nm as the accessible pore radius. The isotherm is very clearly a type IV isotherm with H1 hysteresis and, as in most simulations of smooth pores, shows distinct capillary phase transitions. Our GC-TMMC isotherm is in outstanding agreement with the conventional GCMC isotherm, save for the location of the capillary condensation transition and associated limit of stability which our GC-TMMC simulation predicts at a slightly higher pressure than the GCMC result. This difference is most likely due to the inherent challenges of simulating a fluid near a limit of stability, where the free energy barrier between two phases is extremely low. Despite this minor difference, the results confirm that the

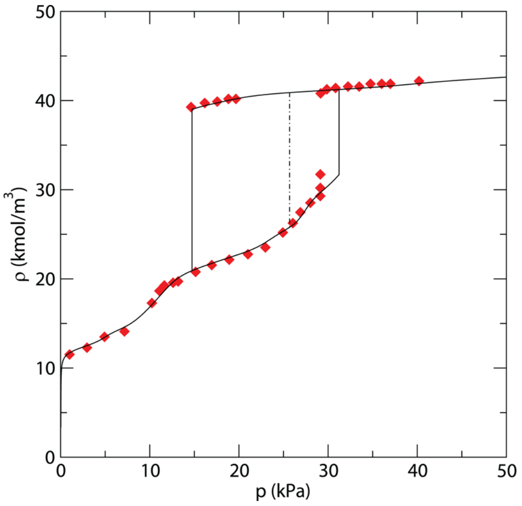

Figure 7. Adsorption isotherm for the Ar−MWCNT system with radius 2.2 nm computed at 87.3 K. The solid black line is the isotherm generated by the GC-TMMC described here. Red symbols are from the GC-MC simulations of Wang et al., from Figure 12 of ref 60. ρ is the average volume of Ar in the pore, based on the total volume definition, and p is the gas pressure in units of kPa. The equilibrium phase transition for systems exhibiting hysteresis is shown by the black dashed line.

GC-TMMC method yields thermodynamic properties consistent with other simulation techniques.

C. Ar–CO_2. For additional validation of GC-TMMC, we now examine the adsorption of Ar in a cylindrical pore bored through solid CO_2, which was previously examined by Panagiotopoulos[65] using Gibbs ensemble MC. For this simulation, we model the adsorptive system using the LJ and CLJ 9-3 potentials mentioned earlier with the interaction parameters given in Table 1. To allow comparison of GC-TMMC results with those of Panagiotopoulos, we set $r_{cut} = 10\sigma_{Ar}$ and set the cylinder's radius to $3\sigma_{Ar} = 1.022$ nm and the axial length to $20\sigma_{Ar} = 6.810$ nm. We ran a GC-TMMC simulation with $N_{min} = 0$ and $N_{max} = 440$ at 95.8 K ($kT/\epsilon = 0.8$) and $z\sigma_{Ar}{}^3 = 0.006392$ to obtain $\Pi(N;\ \mu,\ V,\ T)$. The resultant isotherm is plotted in Figure 8 along with points taken from Figure 7 of ref 65. For this isotherm, the average Ar density in the pore (based on the total volume definition) is plotted versus the bulk gas density, as in ref 65. The relationship between the bulk gas density and imposed chemical potential was obtained from an independent bulk fluid simulation of the LJ fluid using long-range corrections (which will not differ greatly from those of the linear-force shift correction for $r_{cut} = 10\sigma_{Ar}$), the results of which are freely available on the NIST Standard Reference Simulation Website.[84] For the Ar–CO_2 system at 95.8 K, the resultant isotherm exhibits the classic type H1 hysteresis in the IUPAC classification scheme[23] with distinct vapor and liquid branches and vertical capillary phase transitions. The vapor branch of the isotherm is convex to the density (pressure) axis, which is indicative of the weak fluid–solid interaction of the CLJ 9-3 potential[59] and is similar to a type III isotherm.[23] We find that GC-TMMC nearly reproduces the Gibbs ensemble results of Panagiotopoulos with only minor differences. On the liquid branch of the isotherm, GC-TMMC yielded densities slightly below Panagiotopoulos' points but by less than 2%. This deviation is likely within the statistical error of both simulations. Additionally, the Gibbs ensemble results include two points beyond the limits of stability identified by GC-TMMC, one on each of the vapor and liquid branches. The appearance of these points may be attributed to the difficulty of the Gibbs ensemble to adequately sample phases separated by a low free energy barrier, such as near critical points and, in this case, near a limit of stability. We are inclined to ignore this small difference and find that the results are one validation of the GC-TMMC method for generating hysteretic adsorption isotherms.

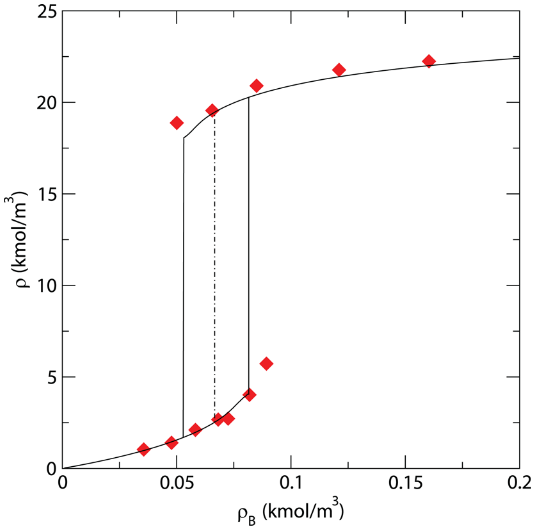

Figure 8. Adsorption isotherm for Ar adsorbing in a cylindrical pore bored through solid CO_2 with radius 1.022 nm at 95.8 K. ρ is the average density of Ar in the pore, based on the total volume definition. ρ_B is the density of the bulk gas for the imposed μ, which was computed in an independent GC-TMMC simulation of the unconfined fluid.[84] The solid line is the isotherm computed using GC-TMMC, and the dashed-dot line is the equilibrium phase transition. Red symbols are simulation points from ref 65 that were computed using Gibbs ensemble Monte Carlo simulation.

Comparison with the results in ref 65 also offers an opportunity to evaluate our identification of the equilibrium phase transition, shown in Figure 8 by the dashed-dot line, since Panagiotopoulos computed the intrapore phase coexistence conditions using a "pore–pore" form of Gibbs ensemble MC. (Direct "pore–pore" equilibrium was possible in this case because the fluid–solid interaction was independent of the system length, allowing for straightforward volume exchange moves. This approach would not be possible for a rigid, atomistically detailed adsorbent which does not allow for volume exchange moves.) In Figure 7 of ref 65, the coexisting densities at the equilibrium phase transition are, approximately, $\rho_v\sigma^3 = 0.059$ and $\rho_l\sigma^3 = 0.46$ (corresponding to 0.63 and 19.3 kmol/m$_3$, respectively). Our GC-TMMC simulation yielded coexistence densities of $\rho_v\sigma^3 = 0.06009(2)$ and $\rho_l\sigma^3 = 0.4626(1)$. The number in parentheses is the uncertainty in the last digit estimated from 95% confidence intervals based on four replicate GC-TMMC simulations with differing initial configurations. Our calculations of the phase coexistence densities are essentially indistinguishable from the Gibbs ensemble results of ref 65. For completeness, we note that the equilibrium phase transition for the Ar–CO_2 system occurs at $\rho_B\sigma^3 = 0.0015850(4)$ or $p/p_0 = 0.26942(6)$. The agreement between our GC-TMMC simulations and earlier Gibbs ensemble MC simulations serves as a confirmation that the two methods yield essentially identical results.

D. CO_2 Adsorption in ZIF-8. Lastly, as a demonstration of the ability of GC-TMMC to model adsorption of a more complicated gas than Ar, we now examine the adsorption of CO_2 by the metal–organic framework ZIF-8, which has been considered as a prospective material for carbon capture applications.[71,73] This application of GC-TMMC represents a more challenging case than the two Ar examples already discussed, since the TraPPE model of CO_2 contains multiple LJ sites and point charges, which necessitate the CBMC and Ewald summation methods mentioned previously. Figure 9 contains the adsorption isotherm obtained via GC-TMMC at 303 K along with both simulation and experimental results from ref 73. We note that the authors of ref 73 used the EPM-2 model of CO_2,[85] which differs from the TraPPE model in its interaction parameters. The resultant isotherm from GC-TMMC is a type I Langmuir-like isotherm,[23] which is expected since the temperature is just below the critical temperature of CO_2 (approximately 306.2 K for TraPPE CO_2,[72] only slightly above that reported for real CO_2, 304.1–304.4 K[86]). This general isotherm trend is identical to the experimental and simulation isotherms reported in ref 73, and our isotherm is essentially indistinguishable from those results up to $p = 1$ bar. For larger pressures, the TraPPE isotherm is slightly lower (5–10%) compared to both the experimental and EPM-2 isotherms from 1 to 20 bar. This is expected, since the LJ parameters of EPM-2 CO_2 are slightly stronger than those of TraPPE CO_2

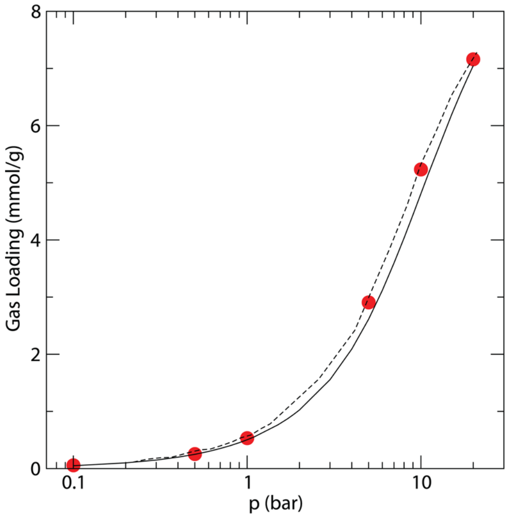

Figure 9. Adsorption isotherm for CO_2 in ZIF-8 at 303 K plotted versus imposed pressure. The loading value is absolute adsorption of CO_2 per unit weight ZIF-8 adsorbent. p, given in bar, is the pressure for the imposed μ, which was computed by GC-TMMC of unconfined CO_2. The solid black line is the isotherm computed here using GC-TMMC. Red symbols are MC simulation points from Figures 2 and 3 of ref 73. The black dashed line is an experimental isotherm given in the same figures of ref 73.

and due to the enhanced packing made possible by the slightly smaller EPM-2 structure. We point out once again that the GC-TMMC isotherm shown in Figure 9 was obtained from a single molecular simulation and that the PNPD could be reweighted to yield additional isotherm points if desired.

VI. SUMMARY AND CONCLUSIONS

In this work, we introduced a GC-TMMC method as an efficient technique for computing various properties of an adsorbed fluid for situations where multiple fluid phases, both stable and metastable, may be present. The key statistical quantity exploited in this work is the PNPD, which is straightforwardly obtained from information about attempted transitions in an otherwise normal MC simulation. The TMMC method selected here is that of Errington and co-workers, which is distinguished from earlier TMMC work by the introduction of a biasing function proportional to the logarithm of the aforementioned PNPD. The self-correcting biasing function encourages the simulation to sample all states uniformly, allowing for satisfactory sampling of N-states with both low and high probability and the accurate construction of the entire PNPD, from which any number of ensemble averages can then be computed.

A particularly attractive feature of GC-TMMC is that a single simulation can provide the necessary information to generate various properties of the adsorptive system for any number of thermodynamic state points. Thus, the PNPD from a single simulation is able to generate an entire adsorption isotherm, locate capillary phase transitions, identify the equilibrium phase transition, and compute other properties. The example applications that we discussed in section V demonstrate that the GC-TMMC method generates adsorption isotherms that are consistent with both expected behavior of adsorbed fluids and previously published simulation results generated by conventional GCMC and Gibbs ensemble simulations of fluid confined in adsorbing pores. Additionally, we demonstrated the ability of GC-TMMC to compute other properties of adsorbed fluids by computing the isosteric heat of adsorption. This property is more challenging to reliably calculate than simple ensemble averages, as it is computed from ensemble fluctuations. The Q_{st} results given here for a family of Ar—MWCNT systems appear to contain less noise than calculations in existing GCMC simulations, which likely follows from the use of the PNPD to compute the necessary ensemble fluctuations.

A valid question that may be asked is whether the GC-TMMC method presents a computational advantage to conventional GCMC, since a particular GC-TMMC simulation is typically run for many more trial moves than an equivalent GCMC simulation. While it is true that one GC-TMMC simulation might require more computational time than, say, the 20 or 50 conventional GCMC simulations used to generate an adsorption isotherm, it is important to keep in mind that a single GC-TMMC simulation provides access to the continuum of state points comprising the entire curve, which is the equivalent of hundreds or thousands of individual GCMC simulations.

The work here presents an initial application of the GC-TMMC method to adsorption problems involving hysteresis, and we anticipate that this method can be widely exploited to improve modeling of adsorption and obtain properties that might be difficult to obtain with conventional or more established forms of MC simulation. For example, if an adsorptive system could support more than two stable states, it is possible that existing MC methods might fail to identify some of those states. In other applications, one can consider the use of temperature-expanded ensembles[66,87,88] and/or temperature reweighting[40] of a macrostate probability distribution to obtain additional temperature-dependent information from a GC-TMMC simulation. This might be used to rigorously search for the hysteresis critical temperature or simply to compute adsorption isotherms and associated properties for more than one temperature, all from a single simulation. Also, since GC-TMMC falls into the class of flat-histogram simulation methods, it is possible to combine its algorithm with other flat-histogram strategies to further improve its efficiency. One such approach is that suggested by Shell et al.[35] in which the Wang—Landau method[32−35] is used to quickly generate the biasing potential while using GC-TMMC to compute the PNPD. Finally, though the present discussion involved fairly simple fluid models (single-site LJ Ar and rigid multisite CO_2), GC-TMMC is no less suited to more complicated fluid models and advanced MC sampling strategies, and modeling of adsorption of complex fluids in various media is just another application that can be considered.

■ AUTHOR INFORMATION

Corresponding Author

*E-mail: daniel.siderius@nist.gov.

Notes

The authors declare no competing financial interest.

■ ACKNOWLEDGMENTS

D.W.S. acknowledges the financial support from a National Research Council postdoctoral research associateship at the National Institute of Standards and Technology.

REFERENCES

(1) Gelb, L. D.; Gubbins, K. E.; Radhakrishnan, R.; Sliwinska-Bartkowiak, M. Phase Separation in Confined Systems. *Rep. Prog. Phys.* **1999**, *62*, 1573−1659.

(2) Rouquerol, F.; Rouquerol, J.; Sing, K. *Adsorption by Powders and Porous Solids*; Academic Press: London, 1999.

(3) Lowell, S.; Shields, J. E.; Thomas, M. A.; Thommes, M. *Characterization of Porous Solids and Powders: Surface Area, Pore Size and Density*; Kluwer: Boston, MA, 2004.

(4) Khoo, H. H.; Tan, R. B. H. Life Cycle Investigation of CO_2 Recovery and Sequestration. *Environ. Sci. Technol.* **2006**, *40*, 4016−4024.

(5) Maginn, E. J. What to Do with CO_2. *J. Phys. Chem. Lett.* **2010**, *1*, 3478−3479.

(6) Meek, S. T.; Greathouse, J. A.; Allendorf, M. D. Metal-Organic Frameworks: A Rapidly Growing Class of Versatile Nanoporous Materials. *Adv. Mater.* **2010**, *23*, 249−267.

(7) Zhou, H. C.; Long, J. R.; Yaghi, O. M. Introduction to Metal Organic Frameworks. *Chem. Rev.* **2012**, *112*, 673−674.

(8) Gubbins, K. E.; Liu, Y. C.; Moore, J. D.; Palmer, J. C. The Role of Molecular Modeling in Confined Systems: Impact and Prospects. *Phys. Chem. Chem. Phys.* **2011**, *13*, 58−85.

(9) Monson, P. A. Understanding Adsorption/Desorption Hysteresis for Fluids in Mesoporous Materials Using Simple Molecular Models and Classical Density Functional Theory. *Microporous Mesoporous Mater.* **2012**, *160*, 47−66.

(10) Yang, Q.; Xue, C.; Zhong, C.; Chen, J. F. Molecular Simulation of Separation of CO2 from Flue Gases in CU-BTC Metal-Organic Framework. *AIChE J.* **2007**, *53*, 2832−2840.

(11) Watanabe, S.; Sholl, D. S. Accelerating Applications of Metal-Organic Frameworks for Gas Adsorption and Separation by Computational Secreening of Materials. *Langmuir* **2012**, *28*, 14114−14128.

(12) Lin, L. C.; Berger, A. H.; Martin, R. L.; Kim, J.; Swisher, J. A.; Jariwala, K.; Rycroft, C. H.; Bhown, A. S.; Deem, M. W.; Haranczyk, M.; Smit, B. In Silico Screening of Carbon-Capture Materials. *Nat. Mater.* **2012**, *11*, 633−641.

(13) Evans, R. Density Functionals in the Theory of Nonuniform Fluids. In *Fundamentals of Inhomogeneous Fluids*; Henderson, D., Ed.; Dekker: New York, 1992; pp 85−175.

(14) de Oliveira, M. J.; Griffiths, R. B. Lattice-Gas Model of Multiple Layer Adsorption. *Surf. Sci.* **1978**, *71*, 687−694.

(15) Marconi, U. M. B.; van Swol, F. Microscopic Model for Hysteresis and Phase Equilibria of Fluids Confined between Parallel Plates. *Phys. Rev. A* **1989**, *39*, 4109−4116.

(16) Kierlik, E.; Monson, P. A.; Rosinberg, M. L.; Sarkisov, L.; Tarjus, G. Capillary Condensation in Disordered Porous Materials: Hysteresis versus Equilibrium Behavior. *Phys. Rev. Lett.* **2001**, *87*, 055701.

(17) Siderius, D. W.; Gelb, L. D. Predicting Gas Adsorption in Complex Microporous and Mesoporous Materials Using a New Density Functional Theory of Finely Discretized Lattice Fluids. *Langmuir* **2009**, *25*, 1296−1299.

(18) Allen, M. P.; Tildesley, D. J. *Computer Simulation of Liquids*; Clarendon: New York, 1987.

(19) Frenkel, D.; Smit, B. *Understanding Molecular Simulation*; Academic Press: San Diego, CA, 1996.

(20) Sarkisov, L.; Monson, P. A. Modeling of Adsorption and Desorption in Pores of Simple Geometry Using Molecular Dynamics. *Langmuir* **2001**, *17*, 7600−7604.

(21) Neimark, A. V.; Ravikovitch, P. I. Adsorption Hysteresis in Nanopores. *Phys. Rev. E* **2000**, *62*, R1493−R1496.

(22) Neimark, A. V.; Ravikovitch, P. I. Capillary Condensation in MMS and Pore Structure Characterization. *Microporous Mesoporous Mater.* **2001**, *44−45*, 697−707.

(23) Sing, K. S. W.; Everett, D. H.; Haul, R. A. W.; Moscou, L.; Pierotti, R. A.; Rouquerol, J.; Siemieniewska, T. Reporting Physisorption Data For Gas/Solid Systems with Special Reference to the Determination of Surface Area and Porosity. *Pure Appl. Chem.* **1985**, *57*, 603−619.

(24) Ravikovitch, P. I.; Neimark, A. V. Experimental Confirmation of Different Mechanisms of Evaporation from Ink-Bottle Type Pores: Equilibrium, Pore Blocking, and Cavitation. *Langmuir* **2002**, *18*, 9830−9837.

(25) Espinal, L.; Wong-Ng, W.; Kaduk, J. A.; Allen, A. J.; Snyder, C. R.; Chiu, C.; Siderius, D. W.; Li, L.; Cockayne, E.; Espinal, A. E.; Suib, S. L. Time-Dependent CO_2 Sorption Hysteresis in a One-Dimensional Microporous Octahedral Molecular Sieve. *J. Am. Chem. Soc.* **2012**, *134*, 7944−7951.

(26) Panagiotopoulos, A. Z. Direct Determination of Phase Coexistence Properties of Fluids by Monte-Carlo Simulation in a New Ensemble. *Mol. Phys.* **1987**, *61*, 813−826.

(27) Panagiotopoulos, A. Z. Direct Determination of Fluid Phase Equilibrium by Simulation in the Gibbs Ensemble: A Review. *Mol. Sim.* **1992**, *9*, 1−23.

(28) Panagiotopoulos, A. Z. Monte Carlo Methods for Phase Equilibria of Fluids. *J. Phys.: Condens. Matter* **2000**, *12*, R25−R52.

(29) Neimark, A. V.; Vishnyakov, A. Gauge Cell Method for Simulation Studies of Phase Transitions in Confined Systems. *Phys. Rev. E* **2000**, *62*, 4611−4622.

(30) Vishnyakov, A.; Neimark, A. V. Studies of Liquid-Vapor Equilibria, Criticality, and Spinodal Transitions in Nanopores by Gauge Cell Monte Carlo Simulations. *J. Phys. Chem. B* **2001**, *105*, 7009−7020.

(31) Neimark, A. V.; Vishnyakov, A. A Simulation Method for the Calculation of Chemical Potentials in Small, Inhomogeneous, and Dense Systems. *J. Chem. Phys.* **2005**, *122*, 174508.

(32) Wang, F.; Landau, D. P. Efficient, Multiple-Range Random Walk Algorithm to Calculate the Density of States. *Phys. Rev. Lett.* **2001**, *86*, 2050−2053.

(33) Wang, F.; Landau, D. P. Determining the Density of States for Classical Statistical Models: A Random Walk Algorithm to Produce a Flat Histogram. *Phys. Rev. E* **2001**, *64*, 056101.

(34) Shell, M. S.; Debenedetti, P. G.; Panagiotopoulos, A. Z. Generalization of the Wang-Landau Method for off-Lattice Simulations. *Phys. Rev. E* **2002**, *66*, 056703.

(35) Shell, M. S.; Debenedetti, P. G.; Panagiotopoulos, A. Z. An Improved Monte Carlo Method for Direct Calculation of the Density of States. *J. Chem. Phys.* **2003**, *119*, 9406−9411.

(36) Desgranges, D.; Delhommelle, J. Evaluation of the Grand-Canonical Partition Function Using Expanded Wang-Landau Simulations. II. Adsorption of Atomic and Molecular Fluids in a Porous Material. *J. Chem. Phys.* **2012**, *136*, 184108.

(37) Fitzgerald, M.; Picard, R. R.; Silver, R. N. Canonical Transition Probabilities for Adaptive Metropolis Simulation. *Europhys. Lett.* **1999**, *46*, 282−287.

(38) Fitzgerald, M.; Picard, R. R.; Silver, R. N. Monte Carlo Transition Dynamics and Variance Reduction. *J. Stat. Phys.* **2000**, *98*, 321−345.

(39) Errington, J. R. Evaluating Surface Tension Using Grand-Canonical Transition-Matrix Monte Carlo Simulation and Finite-Size Scaling. *Phys. Rev. E* **2003**, *67*, 012102.

(40) Errington, J. R. Direct Calculation of Liquid-Vapor Phase Equilibria from Transition Matrix Monte Carlo Simulation. *J. Chem. Phys.* **2003**, *118*, 9915−9925.

(41) Shen, V. K.; Errington, J. R. Metastability and Instability in the Lennard-Jones Fluid Investigated by Transition-Matrix Monte Carlo. *J. Phys. Chem. B* **2004**, *108*, 19595−19606.

(42) Shen, V. K.; Errington, J. R. Determination of Fluid-Phase Behavior Using Transition-Matrix Monte Carlo: Binary Lennard-Jones Mixtures. *J. Chem. Phys.* **2005**, *122*, 064508.

(43) Errington, J. R.; Shen, V. K. Direct Evaluation of Multicomponent Phase Equilibria Using Flat-Histogram Methods. *J. Chem. Phys.* **2005**, *123*, 164103.

(44) Shen, V. K.; Errington, J. R. Determination of Surface Tension in Binary Mixtures Using Transition-Matrix Monte Carlo. *J. Chem. Phys.* **2006**, *124*, 024721.

(45) Errington, J. R. Prewetting Transitions for a Model Argon on Solid Carbon Dioxide System. *Langmuir* **2004**, *20*, 3798−3804.

(46) Chen, H.; Sholl, D. S. Efficient Simulation of Binary Adsorption Isotherms Using Transition Matrix Monte Carlo. *Langmuir* **2006**, *22*, 709−716.

(47) Chen, H.; Sholl, D. S. Examining the Accuracy of Ideal Adsorbed Solution Theory without Curve-Fitting Using Transition Matrix Monte Carlo Simulations. *Langmuir* **2007**, *23*, 6431−6437.

(48) Grzelak, E. M.; Errington, J. R. Computation of Interfacial Properties via Grand Canonical Transition Matrix Monte Carlo Simulation. *J. Chem. Phys.* **2007**, *128*, 014710.

(49) Mohr, P. J.; Taylor, B. N.; Newell, D. B. CODATA Recommended Values of the Fundamental Physical Constants: 2010. *Rev. Mod. Phys.* **2012**, *84*, 1527−1605.

(50) Metropolis, N.; Rosenbluth, A.; Rosenbluth, M. N.; Teller, A.; Teller, E. Equation of State Calculations by Fast Computing Machines. *J. Chem. Phys.* **1953**, *21*, 1087−1092.

(51) Hastings, W. K. Monte Carlo Sampling Methods Using Markov Chains and Their Applications. *Biometrika* **1970**, *57*, 97−109.

(52) Berg, B. A.; Neuhas, T. Multicanonical Ensemble: A New Approach to Simulate First-Order Phase Transitions. *Phys. Rev. Lett.* **1992**, *68*, 9−12.

(53) Papadopoulou, A.; van Swol, F.; Marconi, U. M. B. Pore-End Effects on Adsorption Hysteresis in Cylindrical and Slit-Like Pores. *J. Chem. Phys.* **1992**, *97*, 6942−6952.

(54) Errington, J. R.; Panagiotopoulos, a. Z. Phase Equilibria of the Modified Buckingham Exponential-6 Potential from Hamiltonian Scaling Grand Canonical Monte Carlo. *J. Chem. Phys.* **1998**, *109*, 1093−1100.

(55) Potoff, J. A.; Errington, J. R.; Panagiotopoulos, a. Z. Molecular Simulation of Phase Equilibria for Mixtures of Polar and Non-Polar Components. *Mol. Phys.* **1999**, *97*, 1073−1083.

(56) Nicholson, D.; Parsonage, N. G. *Computer Simulation and the Statistical Mechanics of Adsorption*; Academic Press: London, 1982.

(57) Do, D. D.; Do, H. D.; Nicholson, D. Molecular Simulation of Excess Isotherm and Excess Enthalpy Change in Gas-Phase Adsorption. *J. Phys. Chem. B* **2009**, *113*, 1030−1040.

(58) Do, D. D.; Nicholson, D.; Fan, C. Development of Equations for Differential and Integral Enthalpy Change of Adsorption for Simulation Studies. *Langmuir* **2011**, *27*, 14290−14299.

(59) Siderius, D. W.; Gelb, L. D. Extension of the Steele 10-4-3 Potential for Adsorption Calculations in Cylindrical, Spherical, and Other Pore Geometries. *J. Chem. Phys.* **2011**, *135*, 084703.

(60) Wang, Y.; Do, D. D.; Nicholson, D. Study of Heat of Adsorption across the Capillary Condensation in Cylindrical Pores. *Colloids Surf., A* **2011**, *380*, 66−78.

(61) Wang, Y.; Do, D. D. Personal Communication, 2012. In ref 60, the CNT adsorbent was composed of three concentric CNTs, which was not specified in the text.

(62) Tjatjopoulos, G. J.; Feke, D. L.; Mann, J. A. Molecule-Micropore Interaction Potentials. *J. Phys. Chem.* **1988**, *92*, 4006−4007.

(63) Peterson, B. K.; Walton, J. P. R. B.; Gubbins, K. E. Fluid Behaviour in Narrow Pores. *J. Chem. Soc., Faraday Trans. 2* **1986**, *82*, 1789−1800.

(64) Zhang, X.; Wang, W.; Jiang, G. A Potential Model for Interaction between Lennard-Jones Cylindrical Wall and Fluid Molecules. *Fluid Phase Equilib.* **2004**, *218*, 239−246.

(65) Panagiotopoulos, A. Z. Adsorption and Capillary Condensation of Fluids in Cylindrical Pores by Monte-Carlo Simulation in the Gibbs Ensemble. *Mol. Phys.* **1987**, *62*, 701−719.

(66) Lyubartsev, A. P.; Martsinovski, A. A.; Shevkunov, S. V.; Vorontsov-Velyaminov, P. N. New Approach to Monte Carlo Calculation of the Free Energy: Method of Expanded Ensembles. *J. Chem. Phys.* **1991**, *96*, 1776−1783.

(67) Escobedo, F. A.; De Pablo, J. J. Expanded Grand Canonical and Gibbs Ensemble Monte Carlo Simulation of Polymers. *J. Chem. Phys.* **1996**, *105*, 4931−4394.

(68) Cichowski, E. C.; Schmidt, T. R.; Errington, J. R. Determination of Henry's Law Constants through Transition Matrix Monte Carlo Simulation. *Fluid Phase Equilib.* **2006**, *236*, 58−65.

(69) Singh, J. K.; Errington, J. R. Calculation of Phase Coexistence Properties and Surface Tensions of N-Alkanes with Grand-Canonical Transition-Matrix Monte Carlo Simulation and Finite-Size Scaling. *J. Phys. Chem. B* **2006**, *110*, 1369−1376.

(70) Krekelberg, W. P.; Shen, V. K.; Errington, J. R.; Truskett, T. M. Residual Multiparticle Entropy Does Not Generally Change Sign near Freezing. *J. Chem. Phys.* **2008**, *128*, 161101.

(71) Wong-Ng, W.; Kaduk, J. A.; Espinal, L.; Suchomel, M. R.; Allen, A. J.; Wu, H. High-Resolution Synchrotron X-ray Powder Diffraction Study of Bis(2-Methylimidazolyl)-zinc, C8H10N4Zn (ZIF-8). *Powder Diffr.* **2011**, *26*, 234−237.

(72) Potoff, J. A.; Siepmann, J. I. Vapor-Liquid Equilibria of Mixtures Containing Alkanes, Carbon Dioxide, and Nitrogen. *AIChE J.* **2001**, *47*, 1676−1682.

(73) Perez-Pellitero, J.; Amrouche, H.; Siperstein, F. R.; Pirngruber, G.; Nieto-Draghi, C.; Chaplais, G.; Simon-Masseron, A.; Bazer-Bachi, D.; Peralta, D.; Bats, N. Adsorption of CO_2, CH_4, and N_2 on Zeolitic Imidazolate Frameworks: Experiments and Simulations. *Chem.—Eur. J.* **2010**, *16*, 1560−1570.

(74) Rosenbluth, M. N.; Rosenbluth, A. W. Monte Carlo Calculation of the Average Extension of Molecular Chains. *J. Chem. Phys.* **1955**, *23*, 356−359.

(75) Siepmann, J. I. A Method for the Direct Calculation of Chemical-Potentials in Dense Chain Systems. *Mol. Phys.* **1990**, *70*, 1145−1158.

(76) Siepmann, J. I.; Frenkel, D. Configurational Bias Monte Carlo: A New Sampling Scheme for Flexible Chains. *Mol. Phys.* **1992**, *75*, 59−70.

(77) Laso, M.; De Pablo, J.; Suter, U. W. Simulation of Phase-Equilibria for Chain Molecules. *J. Chem. Phys.* **1992**, *97*, 2817−2819.

(78) Frenkel, D.; Mooij, G. C. A.; Smit, B. Novel Scheme to Study Structural and Thermal-Properties of Continuously Deformable Molecules. *J. Phys.: Condens. Matter* **1992**, *4*, 3053−3076.

(79) Michels, A.; Wijker, H.; Wijker, H. K. Isotherms of Argon between 0C and 150C and Pressures up to 2900 atm. *Physica* **1949**, *15*, 627−635.

(80) Do, D. D.; Do, H. D. Effects of Potential Models in the Vapor-Liquid Equilibria and Adsorption of Simple Gases on Graphitized Thermal Carbon Black. *Fluid Phase Equilib.* **2005**, *235*, 169−177.

(81) Steele, W. A. The Physical Interaction of Gases with Crystalline Solids I. Gas-Solid Energies and Properties of Isolated Adsorbed Atoms. *Surf. Sci.* **1973**, *36*, 317−352.

(82) Ebner, C.; Saam, W. F. New Phase-Transition Phenomena in Thin Argon Films. *Phys. Rev. Lett.* **1977**, *38*, 1486−1489.

(83) Frey, J. T.; Doren, D. J. *Tubegen 3.4*, 2011. http://turin.nss.udel.edu/research/tubegenonline.html.

(84) *NIST Standard Reference Simulation Website*. http://www.nist.gov/mml/csd/informatics_research/srsw.cfm, NIST Standard Reference Database 173.

(85) Harris, J. G.; Yung, K. W. Carbon Dioxide's Liquid-Vapor Coexistence Curve and Critical Properties as Predicted by a Simple Molecular Model. *J. Phys. Chem.* **1995**, *99*, 12021−12024.

(86) *NIST Chemistry WebBook*; Linstrom, P. J., Mallard, W. G., Eds.; NIST Standard Reference Database 69.

(87) Grzelak, E. M.; Errington, J. R. Nanoscale Limit to the Applicability of Wenzel's Equation. *Langmuir* **2010**, *26*, 13297−13304.

(88) Kumar, V.; Sridhar, S.; Errington, J. R. Monte Carlo Simulation Strategies for Computing the Wetting Properties of Fluids at Geometrically Rough Surfaces. *J. Chem. Phys.* **2011**, *135*, 184702.